Chemical Engineering Journal 372 (2019) 1183–1193

Contents lists available at ScienceDirect

Chemical Engineering Journal

journal homepage: www.elsevier.com/locate/cej

Effective steering of charge flow through synergistic inducing oxygen vacancy defects and *p-n* heterojunctions in 2D/2D surface-engineered Bi_2WO_6/BiOI cascade: Towards superior photocatalytic CO_2 reduction activity

Xin Ying Kong[a], Wai Qin Lee[a], Abdul Rahman Mohamed[b], Siang-Piao Chai[a,*]

[a] *Multidisciplinary Platform of Advanced Engineering, Chemical Engineering Discipline, School of Engineering, Monash University, Jalan Lagoon Selatan, Bandar Sunway 47500, Selangor, Malaysia*

[b] *Low Carbon Economy (LCE) Group, School of Chemical Engineering, Universiti Sains Malaysia, Engineering Campus, Seri Ampangan, 14300 Nibong Tebal, Pulau Pinang, Malaysia*

HIGHLIGHTS

- Inducing surface oxygen vacancy defects on 2D/2D coupled Bi_2WO_6/BiOI nanosheets.
- Oxygen vacancies as surface active sites and extend photo-absorption to NIR region.
- *p-n* heterojunctions across 2D/2D motif allow directional migration of charge flow.
- Electrons trapped at oxygen vacancies endow spatial separation of charge carriers.
- Exhibits highest CH_4 yield among all existing 2D BiOI and Bi_2WO_6-based composites.

GRAPHICAL ABSTRACT

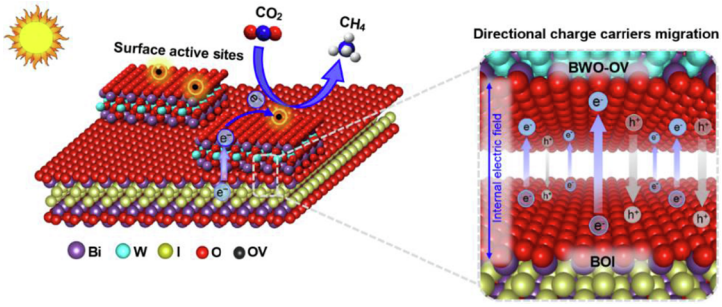

ARTICLE INFO

Keywords:
Photocatalytic CO_2 reduction
Charge flow steering
Oxygen vacancy defects
p-n heterojunction
2D/2D assembly

ABSTRACT

Semiconductor-based photocatalytic CO_2 conversion is a promising and sustainable avenue in response to the anthropogenic climate change and imminent energy crisis, which however is unavoidably impeded by the limited photoabsorption, undesirable recombination of photogenerated charge carriers and insufficient surface active sites on semiconductors. In this study, all these challenges were overcome by selectively and chemically assembly of oxygen-deficient Bi_2WO_6 nanosheets onto BiOI nanosheets, forming a novel surface defect-engineered 2D/2D motif with built-in nanoscale *p-n* heterojunctions. This rational cascade configuration with internal electric field renders ultrafast directional migration and spatial separation of photogenerated charge carriers. Meanwhile, the oxygen vacant sites with abundant trapped electrons serve as the active sites for CO_2 reduction and extend the light absorption of the photocatalytic system to NIR region. Combining these propitious properties, our delineated nanoscale *p-n* heterojunction on the basis of 2D/2D assembly of surface defect-engineered nanosheets presents a new and unprecedented concept for effective generation of charge carriers, directional steering of charge flow and manipulation of surface active sites, which cooperatively lead to superior photocatalytic performance. Notably, our developed oxygen-deficient Bi_2WO_6/BiOI binanosheets exhibit a remarkably high production yield of CH_4, which represents the state-of-the-art visible light-driven CH_4 production activity among all the existing 2D BiOI-based and Bi_2WO_6-based composites.

* Corresponding author.
E-mail address: chai.siang.piao@monash.edu (S.-P. Chai).

https://doi.org/10.1016/j.cej.2019.05.001
Received 29 January 2019; Received in revised form 12 April 2019; Accepted 2 May 2019
Available online 03 May 2019
1385-8947/ © 2019 Elsevier B.V. All rights reserved.

1. Introduction

The ever-increasing carbon dioxide (CO_2) emissions resulted from worldwide consumption of fossil fuels give rise to imminent global energy and environmental crises, which significantly thwart the sustainable development of human societies [1–4]. In the light of this, transformation of the notorious CO_2 greenhouse gas into useful chemicals has particularly captivated global attention. Among all the existing technologies, photocatalytic reduction of CO_2 has been deemed as the most appealing approach as these unwanted CO_2 can be transformed into value-added hydrocarbon fuels through harnessing the clean and inexhaustible solar light [5–10]. This waste-to-fuel technology possesses enormous potential to concurrently alleviate energy and environmental-related issues, thereby achieving a sustainable energy economy [11,12]. Nevertheless, the commercialization of this avenue is still a mirage owing to the CO_2 conversion efficiency is often impeded by the unfavourable electron-hole pairs recombination arisen from the random flow of photoinduced charge carriers after separation [13,14]. In this regard, steering of charge carriers flow, particularly at the nanoscale level, is of paramount significance yet challenging at this stage.

The recent prospers in carbon nitride-related studies have sparked a surge of interest in exploiting novel two-dimensional (2D) layered nanomaterials. Particularly, bismuth oxyiodide (BiOI) has garnered tremendous interest from worldwide researchers in the field of photocatalysis. As the simplest member of Sillén family, its intriguing properties of inexpensiveness and environmental friendliness, optical and chemical stability as well as small energy bandgap (~1.8 eV) for harnessing a broad solar spectrum making it as a prominent photocatalyst of choice [15–18]. However, the major pullback of small bandgap catalysts is the fast recombination of electron-hole pairs, where these charge carriers tend to quench before reaching the semiconductor surface for initiating the redox reactions [19,20]. To address this dilemma, it is of highly desirable to spatially separate these photoinduced electrons and holes to different active sites, thereby prolonging their lifetimes.

To accomplish this, heterostructure assembly of BiOI with other energy band matchable semiconductors seems to be a promising way to manipulate the fates of these charge carriers. Among all, bismuth tungstate (Bi_2WO_6), the simplest member of Aurivillius family which consists of alternating bismuth oxide layers $[Bi_2O_2]_n^{2n+}$ and perovskite-like layers $[WO_4]_n^{2n-}$ [21,22], was chosen to couple with BiOI through the opportune design of heterojunction. In this study, novel oxygen-deficient Bi_2WO_6 nanosheets with surface oxygen vacancy (OV) defects were developed for assembly with BiOI nanosheets. As revealed by our previous works, the presence of OV defects in semiconductor photocatalysts allows the formation of local defect energy levels below conduction band (CB), which can greatly improve the light harvesting capability of semiconductors and effectively trap the photoinduced electrons [23–28]. Furthermore, these OV sites serve as the surface active sites for CO_2 adsorption and activation, where CO_2 molecules adsorbed at the OV sites are spontaneously activated into $\cdot CO_2^-$ radicals, which is the rate-limiting-step of CO_2 reduction [29,30]. It is noteworthy that the novel oxygen-deficient Bi_2WO_6 (Bi_2WO_6-OV) developed in the present study endow well-defined 2D nanosheet structures, which are suitable for assembly with BiOI *via* 2D/2D coupling. In comparison with 0D/2D heterojunction (point-to-face contact) or 1D/2D heterojunction (line-to-face contact), the intimate face-to-face contact embodied by the 2D/2D heterojunction endow large contact surface for easy migration of charge carriers, resulting in an excellent interfacial charge transfer [31].

As widely accepted, the opportune structural design of the nanointerface lays a crucial foundation for steering of interfacial charge kinetics in photocatalytic reactions. In this study, *p-n* heterojunction was constructed between BiOI (*p*-type semiconductor) and Bi_2WO_6-OV (*n*-type semiconductor). Although this *p-n* heterojunction leads to the formation of internal electric field which can accelerate the separation of electron-hole pairs [32], a single strategy with only one charge carriers transfer channel is insufficient to maximize the charge carriers separation. Thus, the OV defects on Bi_2WO_6-OV come into play, where these surface OVs serve as electron trapping sites to thwart the recombination of charge carriers. Through this, we demonstrate an unprecedented electron transportation pathway in this work, where photoinduced electrons directionally migrate from the photoexcited BiOI to CB of Bi_2WO_6-OV *via p-n* heterojunction, which then followed by second-step electron transfer from CB of Bi_2WO_6-OV to the local defect states. Under these circumstances, the OV sites served as electron-trapping and accumulated sites. Moreover, adsorption of CO_2 molecules on OVs is energetically favourable, where these CO_2 molecules can be spontaneously activated through accepting electrons from the OVs. Additionally, the photoresponse of the photocatalytic system is extended to NIR region, which allows more electron-hole pairs generated for participation in redox reactions.

Making full use of these advantageous characteristics, our developed 2D/2D surface defect-engineered Bi_2WO_6/BiOI cascade with built-in *p-n* heterojunctions presents as an elegant example for effective generation, separation, transportation and consumption of charge carriers. Since the OV sites are the active sites for photocatalytic CO_2 reduction process, our artificially inducing OV defects on Bi_2WO_6 allows us to tune and manipulate these surface active sites at a nanoscale level. To the best of our knowledge, there is no previous work reports on the coupling of oxygen-deficient Bi_2WO_6 with BiOI. In fact, study on the roles of OV defects played in nanocomposites is very limited. As far as we know, this is the first research work which successfully demonstrates the synergistic effects of *p-n* heterojunction and oxygen vacancy defects in photocatalytic CO_2 reduction. Our careful design and nanoscale-level control of architectures and electronic structures endow this novel 2D/2D Bi_2WO_6-OV/BiOI photocatalyst to surpass the photoactivities of other existing 2D BiOI and Bi_2WO_6-based photocatalytic system, without involving any rare earth or noble metals. We believe that our findings may shed some mechanistic insights into broad solar spectrum harvesting for effective steering and consumption of charge carriers, thus paving new ways for the exploration of highly efficient and cost-effective photocatalysts.

2. Materials and methods

2.1. Materials

Bismuth (III) nitrate pentahydrate, $Bi(NO_3)_3{\cdot}5H_2O$ (≥98.0%), potassium iodide, KI (≥99.0%), sodium hydroxide, NaOH (≥98.5%), glacial acetic acid, CH_3COOH (≥99.85%) and oleylamine, $C_{18}H_{35}NH_2$ (≥99.0%) were procured from Sigma Aldrich. Sodium tungstate dihydrate, $Na_2WO_4{\cdot}2H_2O$ (≥99.0%) was obtained from Merck whereas ethanol, C_2H_5OH (≥99.8%) and acetone, CH_3COCH_3 (AR grade) were purchased from Friendemann Schmidt Chemical. All the chemical reagents were of analytical grade and used as received without further purification. Deionized water (resistivity ≥ 18.2 MΩ cm) was used throughout the course of the experiment.

2.2. Synthesis of BiOI nanoplates (BOI)

Typically, 4 mmol of $Bi(NO_3)_3{\cdot}5H_2O$ was dispersed in 100 mL of deionized water mixed with 10 mL of glacial acetic acid under vigorous stirring at ambient temperature. Next, the resulting solution was promptly added into a 100 mL aqueous solution containing 4 mmol of KI. The mixture was stirred for another 40 min and followed by aging for 4 h. Finally, the precipitate was collected, washed repeatedly with ethanol and deionized water, and dried in a vacuum oven at 60 °C for overnight.

2.3. Synthesis of oxygen-deficient Bi_2WO_6 nanosheets (BWO-OV)

In general, 2 mmol of $Na_2WO_4{\cdot}2H_2O$ was dissolved in 80 mL of deionized water and the transparent solution was added slowly into 60 mL of absolute ethanol containing 4 mmol of $Bi(NO_3)_3{\cdot}5H_2O$. Subsequently, 20 mL of oleylamine was rapidly added and the mixture solution was vigorously stirred for 1 h at ambient temperature. Following that, the resulting mixture was transferred into a 200 mL Teflon-sealed autoclave and maintained at 200 °C for 8 h. After completion of reaction, the autoclave was allowed to cool naturally to room temperature. The resulting precipitate was filtered, washed thoroughly with acetone, ethanol and deionized water, and lastly dried in a vacuum oven at 60 °C for overnight. The collected sample was denoted as BWO-OV.

2.4. Assembly of BWO-OV onto BOI

The coupling of BOI and BWO-OV was through a simple self-assembly approach. Firstly, 0.4 g of BOI was dispersed in a three-neck flask containing 120 mL of deionized water under ultrasonication to obtain a homogenous solution. Meanwhile, a pre-calculated amount of BWO-OV was dispersed in 30 mL of acetone under ultrasonication, which was then added dropwise into the previous solution under vigorous stirring. Subsequently, the mixture solution was deoxygenated by bubbling nitrogen gas for 60 min at ambient temperature, and followed by reflux at 50 °C for 6 h under a constant stirring rate of 200 rpm with continuous nitrogen gas flow. The resulting mixture was allowed to cool naturally to room temperature, and the precipitate was collected and subjected to vacuum drying at 60 °C for overnight. For optimization, various weight percentages of BWO-OV were studied, including 2, 4, 6, 8, 10, 15 and 20 wt%, and the samples were abbreviated as *x*BWO-OV/BOI, where x = 2, 4, 6, 8, 10, 15 and 20, respectively. For control experiments, pristine Bi_2WO_6 without oxygen vacancies (BWO-P) was prepared by annealing BWO-OV in an air-rich atmosphere at 400 °C for 4 h to heal the oxygen vacant sites. Then, 8 wt% of BWO-P was assembled with BOI under the identical experimental conditions.

2.5. Materials characterization

The surface morphology of the as-synthesized samples was studied by a Hitachi SU 8010 field emission scanning electron microscopy (FESEM). Transmission electron microscopy (TEM) images, high-resolution (HRTEM) images, selected-area electron microscopy (SAED) diffraction patterns and energy-dispersive X-ray spectroscopy (EDX) mapping of the samples were acquired using a TECNAI G2 F20 TEM at an accelerating voltage of 200 kV. The TEM specimens were prepared by dropping the sample suspension in ethanol onto a carbon-coated copper grid. The powder X-ray diffraction (XRD) pattern of the samples were recorded on a Bruker D8 Discover X-Ray diffractometer with Ni-filtered Cu K_α radiation (λ = 0.15406 nm) over a diffraction angle range of 2θ = 20–80° at a scan rate of 0.02 s^{-1}, accelerating voltage of 40 kV and applied current of 40 mA. The X-ray photoelectron spectroscopy (XPS) analysis were performed by a scanning X-ray microprobe PHI Quantera II (Ulvac-PHI, INC.) equipped with a monochromatic Al-K_α X-ray source ($h\nu$ = 1486.6 eV), which operated at an ultra-vacuum (2.4×10^{-6}) environment. Prior to deconvolution, calibration was performed where all the binding energies were charged corrected by setting the adventitious carbon signal (C 1s) to 284.6 eV. Lastly, the optical properties of the photocatalyst samples were examined by an Agilent Cary 100 Ultraviolet–visible (UV–Vis) spectrophotometer where the light absorption spectra of the samples were measured in the wavelength range of 200–800 nm.

2.6. Photoelectochemical analysis

The photoelectrochemical (PEC) properties of the photocatalyst samples were evaluated using a CHI 6005E electrochemical workstation. The standard three-electrode quartz cell setup consists of a Pt rod and Ag/AgCl, which served as counter and reference electrode, respectively. The working electrode was acquired by drop-casting the samples in ethanol suspension (5 mg/mL) onto a fluorine-doped tin oxide (FTO) glass slide with an electroactive area of 1 cm^2. A 0.5 M Na_2SO_4 aqueous solution was utilized as the electrolyte. Throughout the PEC measurement, a 500 W Xenon arc lamp (CHF-XM-500 W) equipped with an UV cut-off filter (to remove $\lambda < 400$ nm) was used as the exciting visible light source.

2.7. Photocatalytic CO_2 reduction experiments

To determine the amount of CH_4 evolved from CO_2 photoreduction experiment, the reaction was conducted in a continuous gas phase reactor which was maintained at atmospheric pressure and ambient temperature. To simulate visible light, a 500 W Xenon arc lamp (CHF-XM-500 W) equipped with an UV cut-off filter (to remove $\lambda < 400$ nm) was utilized as the light source. The experimental setup and incident light spectrum were depicted in Fig. S1. Firstly, the photocatalyst sample was uniformly coated on glass rods, which were then inserted into quartz columns occurring in two consecutive series. A high purity source of CO_2 (99.999%) was bubbled through H_2O to obtain a gas mixture of CO_2/H_2O and the gas mixture was directed to the reaction system. Prior to the experiment, the quartz columns loaded with coated photocatalyst sample were purged with the CO_2/H_2O gas mixture at high flowrate (50 mL/min) for 30 min to evacuate excess air from the system and to ensure adsorption-desorption equilibrium was attained on the surface of photocatalyst. Subsequently, the gas mixture flowrate was adjusted to 5 mL/min and light was supplied from the top of reactor vessel. Throughout the course of experiment, the entire reaction system was shielded inside a black box to avoid light interference from the surroundings. The gaseous product evolved from the reaction was analyzed at every 1 h interval for continuous 8 h using a gas chromatography (Agilent 7820A) equipped with flame ionized detector (FID) and thermal conductivity detector (TCD). The resultant CH_4 yield was quantified using the following equation:

$$\text{CH}_4 \text{ yield } (\mu\text{mol } g^{-1}\ h^{-1}) = \frac{(C_{final,\ CH_4} - C_{initial,\ CH_4}) \times \text{volumetric flow rate of product gas}}{\text{Mass of photocatalyst used (g)}} \quad (1)$$

The apparent quantum yield (AQY) for photocatalytic CH_4 evolution was measured under similar experimental conditions, except that a 420 nm band-pass filter was used instead of the UV cut-off filter. The AQY of the reaction was calculated according to the following equation:

$$\text{AQY (\%)} = \frac{\text{number of reacted electrons}}{\text{number of incident photons}} \times 100\% = \frac{8 \times \text{number of CH}_4 \text{ produced}}{\text{number of incident photons}} \times 100\% = \frac{8\nu t N_A}{I\lambda S t\left(\frac{1}{hc}\right)} \times 100\% \quad (2)$$

where ν is the average CH_4 production rate (mol/s), t is reaction time (s), N_A is Avogadro's constant of 6.0221×10^{23} (mol^{-1}), I is intensity of incident light (W/cm^2), λ is wavelength of incident light (nm), S is irradiation area (cm^2), h is Planck constant of 6.6261×10^{-34} (J s) and c is speed of light which is 3×10^8 m/s.

3. Results and discussion

3.1. Materials characterization

The morphology and microstructure of the samples were examined by FESEM and TEM. From the FESEM image of bare BiOI (abbreviated as BOI) (Fig. 1A), 2D nanosheet-shaped structures with lateral length of

micrometer-sized are clearly observed. HRTEM image (Fig. 1B) taken from the in-plane region of BOI discloses two sets of crystal lattice fringes perpendicular to each other with an equal spacing of 0.283 nm, which correspond to the (1 1 0) atomic plane of BiOI perpendicular to the (0 0 1) plane. As shown by the SAED pattern (Fig. 1C), the interfacial angle between the adjacent spots was measured as 45°, which agrees with the theoretical angle between (1 0 0) and (1 1 0) planes. Thus, this set of SAED diffraction spots can be well-indexed to the [0 0 1] zone axis of tetragonal BiOI, confirming that the as-developed BOI nanosheets were predominantly exposed with {0 0 1} facets on both the top and bottom surfaces, as illustrated in Fig. 1D, and its corresponding crystal structure shown in Fig. 1E.

For oxygen-deficient Bi_2WO_6 (denoted as BWO-OV), FESEM image (Fig. 1F) divulges its nanosheet-shaped structures with in-plane size of 100–200 nm and slightly curved inward edges. From the HRTEM image (Fig. 1G), the distinct lattice fringes with 0.272 and 0.273 nm interplanar spacings are ascribed to the (0 2 0) and (2 0 0) atomic planes of Bi_2WO_6, respectively, which indicates that the top and bottom surfaces of BWO-OV are also of {0 0 1} facets. This is further proven by SAED pattern (Fig. 1H), where the diffraction spots are indexed to the [0 0 1] zone axis of Bi_2WO_6. As shown by the schematic illustration of crystal orientation (Fig. 1I) and crystal structure modelled by the visualization for electronic and structural analysis (VESTA) (Fig. IJ), our developed BWO-OV nanosheets are made up from highly exposed {0 0 1} facets, which consist of high density of terminal oxygen atoms. With the presence of oleylamine – a mild reducing agent in the synthesis of BWO-OV, the surface oxygen atoms were selectively removed from the BWO, leaving oxygen-deficient defects on the sample surface. The presence of OV defects on BWO-OV will be further examined and discussed later.

Of note, {0 0 1} facet is the most reactive facet for both Bi_2WO_6 and BiOI [33–35]. Thus, the strategic coupling of highly active {0 0 1}-faceted binanosheets is favourable, as it endows abundant energetic charge carriers to transfer across the heterojunction. In addition, theoretical calculations revealed that the CO_2 photoreduction process is energetically favoured over the {0 0 1} facets of Bi_2WO_6 [35]. The FESEM image (Fig. 1K) of BOI with 8 wt% loading of BWO-OV (abbreviated as BWO-OV/BOI) delineates a 2D/2D heterostructured architecture, where several small nanosheets are tightly anchored on a large BOI can be obviously observed from the FESEM image, suggesting that the dominant exposed facets remain unchanged after the assembly process. Notably, the distinguished and coherent interfaces between BOI and BWO-OV (Fig. 1L) indicates the formation of intimate interfacial contact, which facilitates the migration of photogenerated charge carriers across the 2D/2D interfacial domain. Elemental mapping images (Fig. 1M–P) reveal the coexistence of Bi, O, W and I elements in the composites, where the small and large nanosheets are identified as BWO-OV and BOI, respectively. The well overlapping of W element with I element in the contact region of BWO-OV and BOI further affirms the formation of intimate 2D/2D interaction in the composite.

XRD analysis was employed to study the crystallographic structures of the samples. As shown in Fig. 2A, the XRD peaks of BOI can be readily indexed to the tetragonal phase of BiOI (JCPDS no. 73-2062)

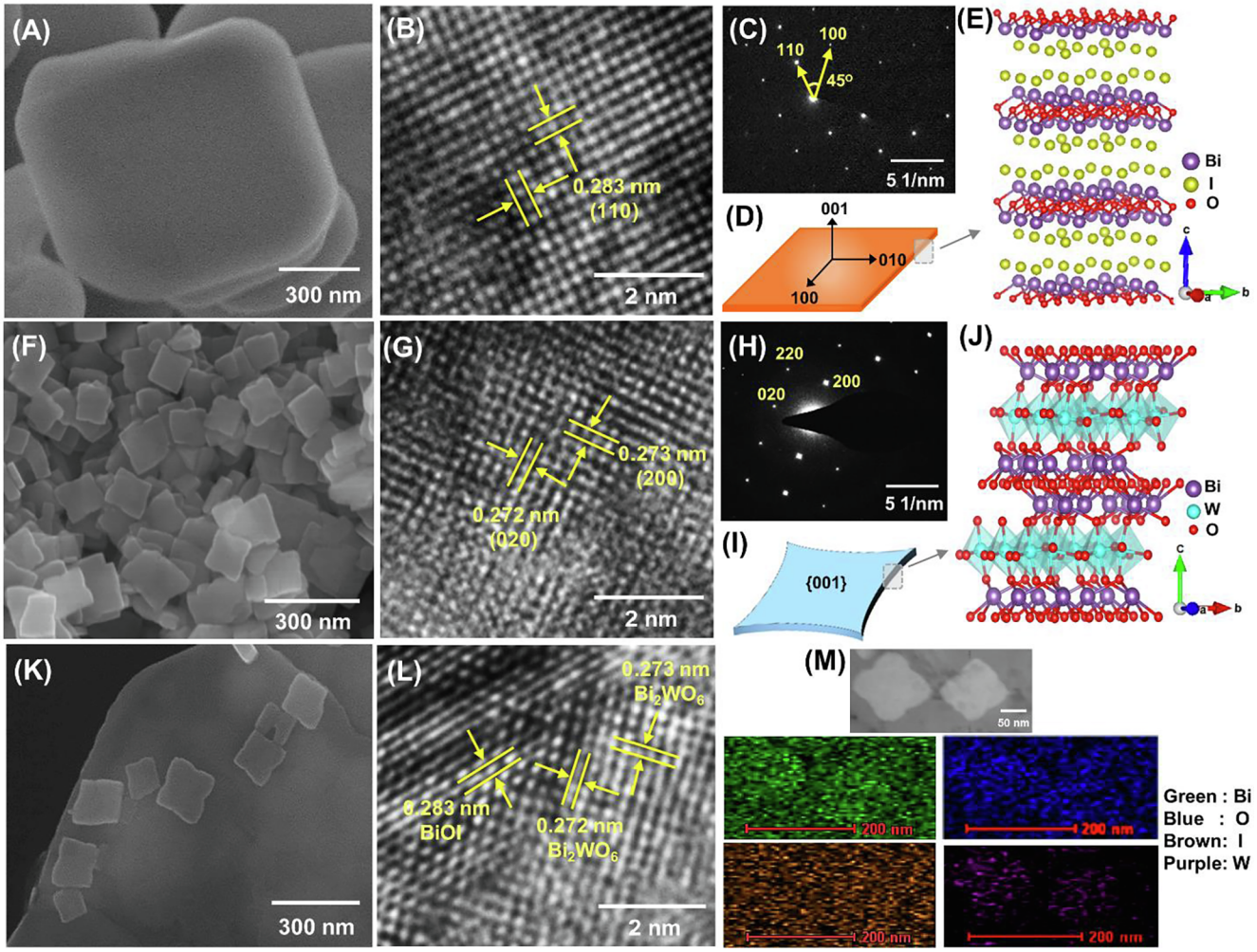

Fig. 1. (A, F) FESEM images, (B, G) top-view HRTEM images, (C, H) SAED patterns, (D, I) crystal orientations and (E, J) crystal structures of BOI (A–E) and BWO-OV (F–J). (K) FESEM image, (L) top-view HRTEM image and (M–P) EDS mapping (inset shows the corresponding STEM image) of binary BWO-OV/BOI composites (K–P).

and those of BWO-OV are ascribed to the orthorhombic phase of Bi_2WO_6 (JCPDS no. 73-1126). It is worth mentioning that the relative intensity of (2 0 0) peak to (1 1 3) peak at 32.8° and 28.3°, respectively, exhibited by the BWO-OV is 0.697, which is much higher than the standard ratio of 0.185 as indicated in JCPDS no. 73-1126 database. This elucidates that our prepared BWO-OV grows anisotropically along the (0 0 1) plane [35,36], which are in line with our HRTEM and SAED observations. For the binary BWO-OV/BOI composite with 8 wt% loading of BWO-OV, the featured peaks of BWO-OV can be obviously seen, which further evidenced the successful assembly of BWO-OV on BiOI. Furthermore, the higher the loading of BWO-OV, the stronger the characteristic peaks of BWO-OV in the composites (Fig. S2).

To determine the elemental composition and atomic chemical environment the samples, XPS analysis was conducted. The XPS survey spectrum (Fig. 2B) revealed the co-existence of Bi, O, W and I elements in the BWO-OV/BOI, which is well agreed with the chemical composition of the sample. To affirm the presence of OV defects in the BWO-OV, the control sample, pristine Bi_2WO_6 without OV (BWO-P) was prepared by annealing BWO-OV in an air rich atmosphere at 400 °C for 4 h to heal the oxygen vacant sites. The high-solution Bi 4f spectrum of BWO-P (Fig. 2C) displayed two peaks at 159.3 and 164.7 eV, which are assigned to the Bi $4f_{7/2}$ and Bi $4f_{5/2}$ in the Bi^{3+} chemical state, respectively [37]. In comparison, a significant 0.4 eV shift to the region of lower binding energy and formation of two additional small peaks which correspond to the $Bi^{(3-x)+}$ chemical state were observed for BWO-OV. This phenomenon is classically attributed to the presence of OV defects, where localized electrons are trapped at the OV sites which leads to the partial reduction of neighbouring Bi atoms [38]. It is noteworthy that the characteristic peaks of $Bi^{(3-x)+}$ can also be seen for BWO-OV/BOI sample, suggesting that the OV defects in BWO-OV retained in the composites. For the O1s spectra of BWO-P and BWO-OV (Fig. 2D), peaks centred at 530.0, 530.6 and 531.9 eV are assigned to the crystal lattice oxygen atoms in Bi-O, W-O and surface adsorbed H_2O, respectively. In comparison to BWO-P, BWO-OV displayed an

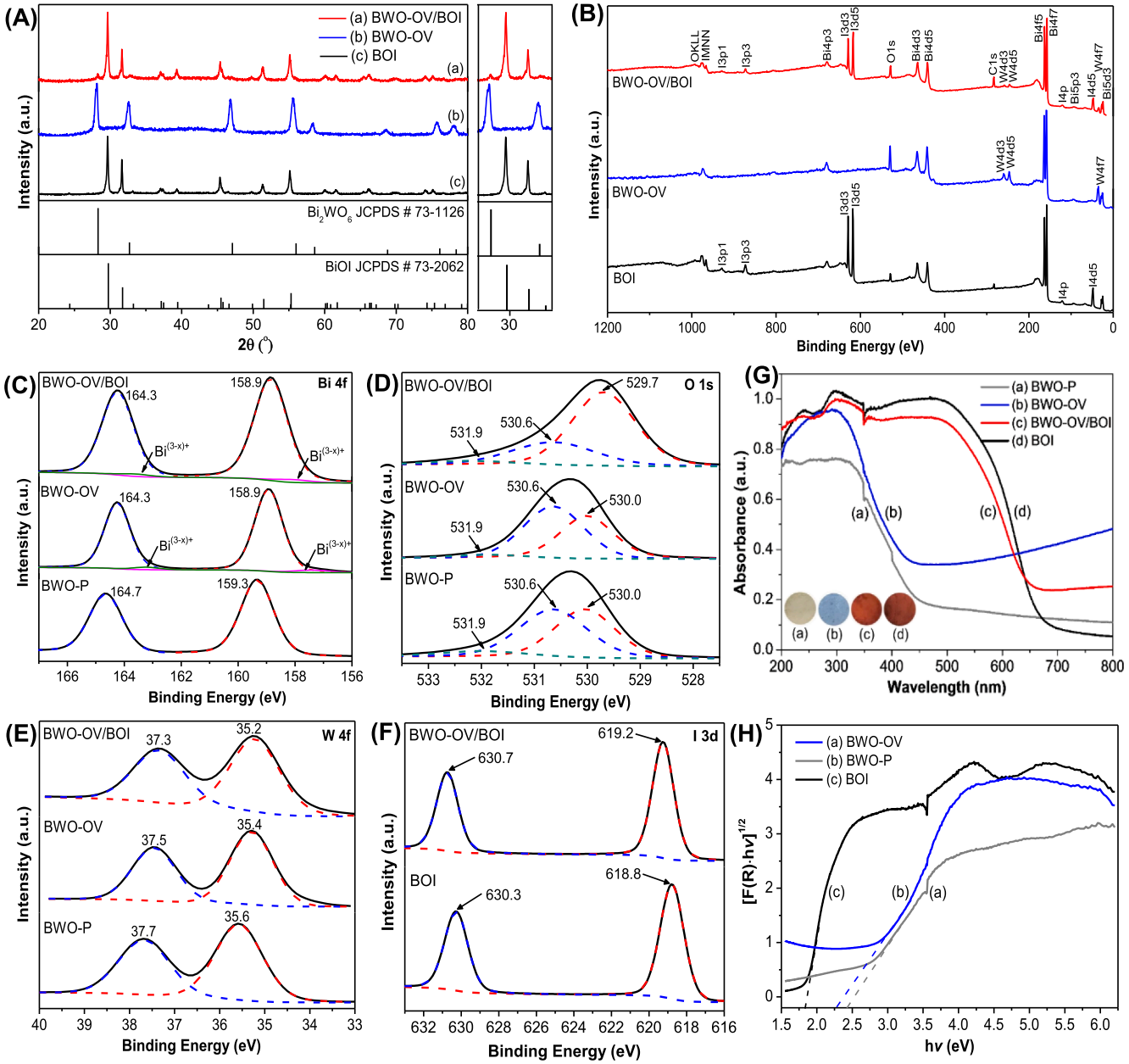

Fig. 2. (A) XRD pattern, (B) XPS survey spectra, (C) high-resolution Bi 4f, (D) O1s, (E) W 4f, (F) I 3d spectra, (G) UV–Vis absorption spectra (insets show the colours of samples) and (H) Tauc plots of the as-prepared photocatalysts.

appreciable decrease in B-O peak, manifesting that the OV defects were mainly formed from the elimination of surface oxygen atoms from Bi-O layers. For BWO-OV/BOI, a pronounced increase in Bi-O peak was contributed by the $[Bi_2O_2]^{2+}$ slabs in BiOI. The W 4f spectrum of BWO-P (Fig. 2E) comprises of two spin-orbit doublets at 35.6 and 37.7 eV, which are ascribable to the W $4f_{7/2}$ and W $4f_{5/2}$ core levels in the W^{6+} chemical state, respectively [39]. With the presence of OVs, BWO-OV exhibited a noticeable 0.2 eV shift to lower binding energy, resulting from the change in electron density. After the incorporation with BiOI, a further reduction in binding energies was observed for BWO-OV/BOI composite. Specifically, a negative shift in binding energy indicates an increase in electron density and *vice versa* [40,41]. Thus, the electron migration pathway in the composites can be determined from the shifting of XPS binding energy. In this case, the negative shift of W 4f state implies that BWO-OV acted as an electron acceptor in the BWO-OV/BOI composites. To further unveil the electron transportation direction, high-resolution I 3d spectra of solitary BOI and BWO-OV/BOI composite were also examined. Based on the I 3d spectrum of BOI (Fig. 2F), the peaks at 618.8 and 630.3 eV respectively correspond to the I $3d_{5/2}$ and $3d_{3/2}$ of I^- chemical state [42]. For the I 3d states of BWO-OV/BOI composite, a significant 0.4 eV shift to higher binding energy was clearly seen, which infers a decrease in electron density. Combining the observations of binding energy shifting for W 4f and I 3d states, the results indicate that the photogenerated electrons migrated from BOI to BWO-OV during photoexcitation process, where BOI served as electron donor and BWO-OV served as electron acceptor. The detailed mechanism of electron transportation pathway in our 2D/2D binary BWO-OV/BOI composites will be further elaborated later.

The optical properties of the as-developed samples were evaluated by UV–Vis diffuse reflectance spectroscopy (UV–Vis DRS). As displayed in Fig. 2G insets, BWO-P was yellowish-white in colour whereas BWO-OV appeared as sky blue in colour. The stark alteration in colour was reflected in the UV–Vis absorption spectra (Fig. 2G), in which BWO-OV exhibited a much intense visible light absorption, and even extended to the near-infrared (NIR) region. The long absorption tail of BWO-OV provided indisputable evidence for the presence of high-density surface defects in BWO-OV, where the formation of absorption tail was due to the sub-band excitation of electrons from OV-induced mid-gap states to the CB of photocatalyst. Similar phenomenon was also reported in the literature [38,43]. Moreover, closer inspection shows that the absorption edge of BWO-OV was red-shifted, accompanying by a bandgap narrowing. Based on the Tauc plots in Fig. 2H, the bandgaps of BWO-P and BWO-OV were measured to be *ca.* 2.43 and 2.26 eV, respectively. On the other hand, BOI was observed to display strong photoresponse to both UV and visible light regions. The absorption edge of BOI was found to be *ca.* 675 nm, corresponding to the bandgap energy of 1.84 eV (Fig. 2G and H). Combining the propitious features of both BOI and BWO-OV, our 2D/2D binary BWO-OV/BOI composite was found to be photoresponsive over broad solar spectrum, ranging from UV to NIR region. This is highly desirable as the strong light harvesting ability of BWO-OV/BOI is anticipated to produce more electron-hole pairs to take part in the reactions, leading to an improved photocatalytic performance.

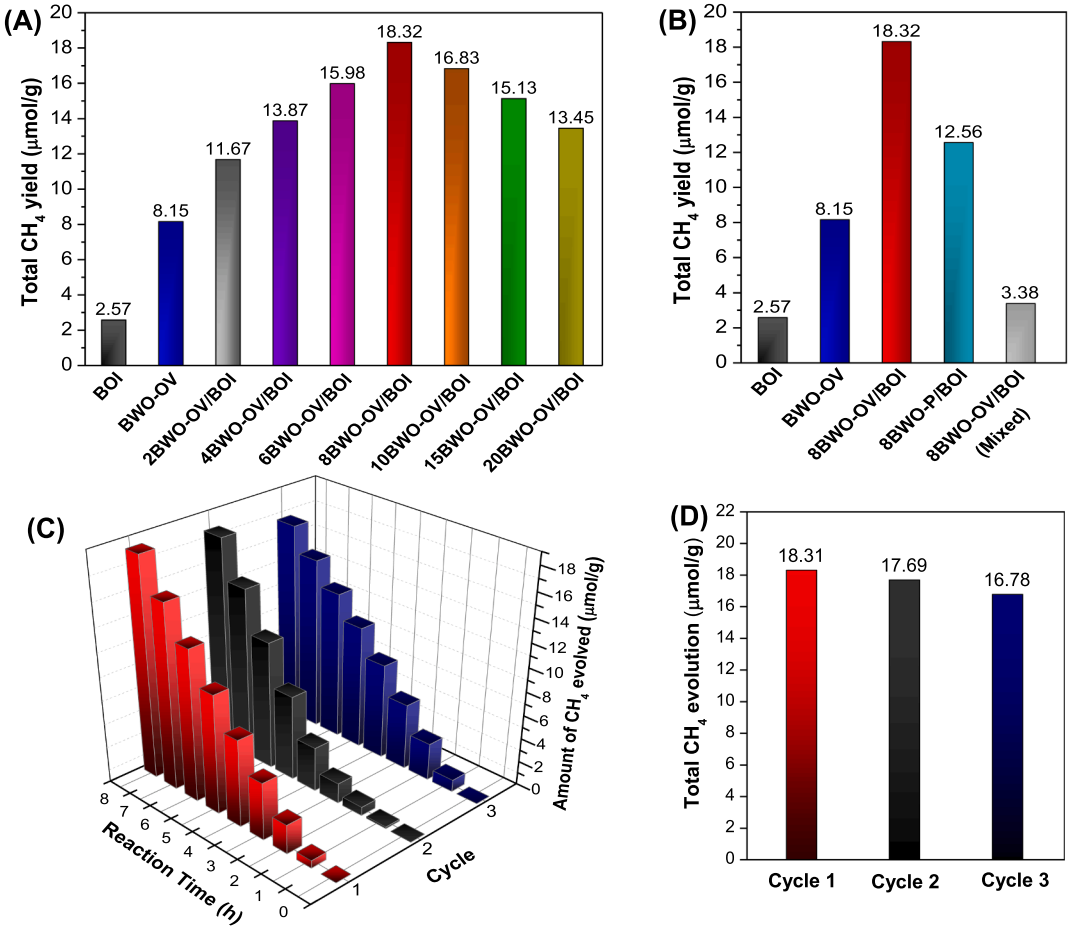

Fig. 3. (A) and (B) Total yield of CH_4 production after 8 h of visible light-driven CO_2 photoreduction over the as-developed samples. Photostability tests of 8BWO-OV/BOI under identical experimental conditions: (C) time course of CH_4 evolution and (D) accumulated CH_4 yield from each test cycle.

3.2. Photocatalytic CO_2 reduction and mechanism for enhanced performance

The photocatalytic performance of our as-developed samples was evaluated by the gas-phase photoreduction of CO_2 experiments conducted at ambient temperature and atmospheric pressure. A 500 W Xenon arc lamp quipped with UV cut-off filter ($\lambda > 400$ nm) was employed as the visible light source. A series of control experiments was systematically performed under several conditions, including: (1) without CO_2 source (under N_2/H_2O flow); (2) without H_2O (under dry CO_2 flow); and (3) without light illumination on the samples. In all these cases, no appreciable amount of carbon-related product was detected (Fig. S3), confirming that the CH_4 product yield was originally stemmed from the photocatalytic reactions and the possibility of decomposition of carbon residuals or self-photolysis can be confidently ruled out. Fig. 3A shows the total production yield of CH_4 over the samples after 8 h of photocatalytic CO_2 reduction under visible light illumination. At the optimal loading of 8 wt% BWO-OV, the BWO-OV/BOI composite manifested a total CH_4 yield of 18.32 μmol/g, which is distinctly higher than the existing 2D BiOI-based and Bi_2WO_6-based photocatalytic systems (Table S1). Significantly, the 8BWO-OV/BOI hybrid photocatalyst exhibited a remarkable 2.2 and 7.1-fold enhancement over the solitary BWO-OV and BOI photocatalysts, which manifests that heterojunction was formed between the interfaces of BOI and BWO-OV. This was also proven by the minimal production of CH_4 attained from the physical mixtures of BWO-OV and BOI (abbrev. as BWO-OV/BOI-Mix) (Fig. 3B), implying that the formation of heterojunction is necessary to lead to a stark improvement in photoactivities. On the other hand, another control sample of pristine Bi_2WO_6 without OV defects and BOI hybrid (denoted as 8BWO-P/BOI) was also prepared and its photoactivity was investigated. In comparison to 8BWO-OV/BOI, the photocatalytic performance of 8BWO-P/BOI was much lower, verifying that OVs play a crucial role in enhancing the photoactivity. These findings revealed that our rational design of BWO-OV/BOI with co-existence of heterojunction and surface disorder defects can integratively lead to boosted photocatalytic performance. More importantly, 8BWO-OV/BOI composite exhibited superior photostability, where it maintained about 92% of reactivity after three consecutive test cycles of CO_2 reduction reactions under the identical experimental conditions (Fig. 3C and D). As reported in the literature [4] and our previous work [44], the decrease of photoactivity over reaction time is a common phenomenon for oxygen-deficient semiconductor owing to the re-oxidation of oxygen-depleted surface by free O atoms generated from the dissociation of CO_2 molecules. In contrast, our binary BWO-OV/BOI nanocomposite possesses robust recyclability and suitable for repeated applications. Other than CH_4, a large amount of carbon monoxide (CO) was also produced from the reaction over 8BWO-OV/BOI, accompanying with the formation of oxidation product – oxygen (O_2), as depicted in Fig. S4.

The superior performance of our developed BWO-OV/BOI hybrid photocatalyst has ignited our interest to unravel how BWO-OV assisted BOI in photocatalytic reactions. To this, a series of characterization was systematically performed for in-depth exploitation of the origin underlying factors. Primarily, transient photocurrent responses of the samples were examined through the on-off cycles of intermittent visible light irradiation. In a typical analysis, the photoinduced electrons are transferred to the back contact to generate photocurrent responses [45–47]. Meanwhile, the holes migrate to the interface between photocatalyst and electrolyte, which are then captured by the reduced species present in the electrolyte during photo-irradiation. Considering that the preparation of electrolyte and electrodes were identical for each measurement, the photocurrent intensity exhibited by the samples reflects the efficiency of generation and separation of the photoinduced charge carriers [48,49]. As shown in Fig. 4A, BOI exhibited minimal photocurrent responses, which is attributed to its narrow energy bandgap leading to the flash recombination of charge carriers. For the case of BWO-P/BOI, the 2D/2D configuration with intimate contact allows effective shuttling of photogenerated electrons across the

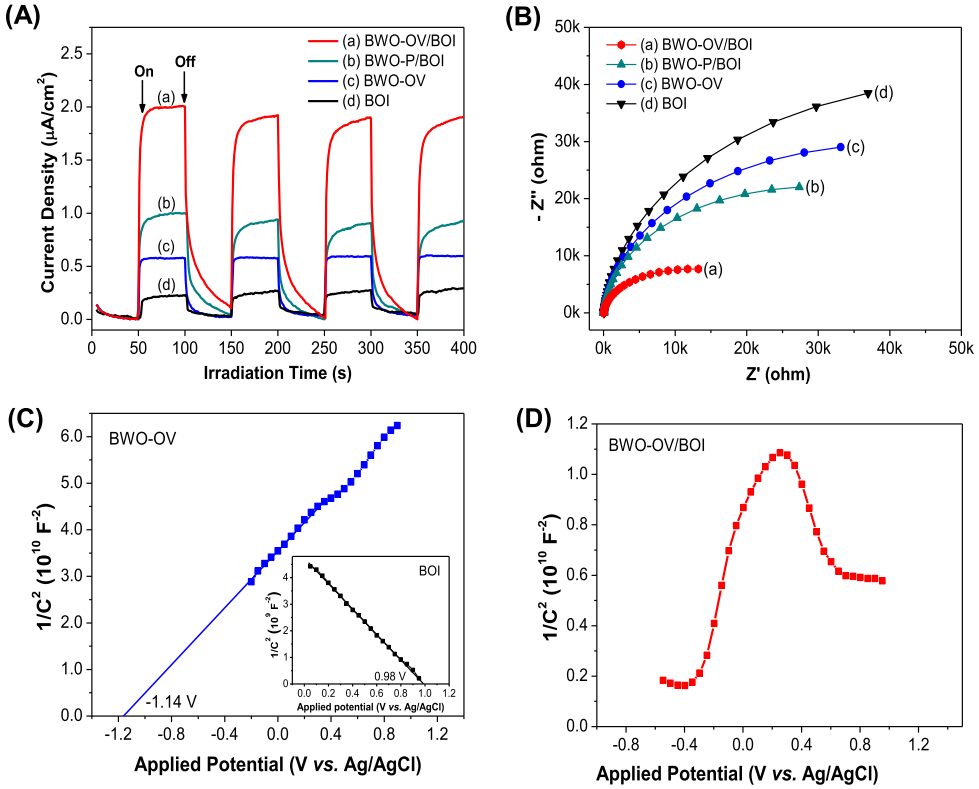

Fig. 4. (A) Transient photocurrent responses and (B) EIS Nyquist plots of the as-developed samples. Mott Schottky plot of (C) BWO-OV (inset shows the plot of BOI) and (D) BWO-OV/BOI composite.

heterojunction, resulting in an enhanced photocurrent intensity. By replacing BWO-P with BWO-OV for assembly with BOI, a pronounced improvement in the photocurrent responses was obviously seen. This manifests the pivotal roles of OV defects as electron trapping sites to thwart the recombination of charge carriers, rendering more charge carriers to take part in the photocatalytic reactions. Fig. S5A shows the photocurrent responses of *x*BWO-OV/BOI composites with different loadings of BWO-OV. It is noteworthy that the photocurrent intensity of all the samples was in the same order as their exhibited photoactivity during CO_2 reduction experiments. This suggests that the separation of electron-hole pairs is a decisive factor for the performance of photocatalysts, further highlighting the importance of our current work which focuses on opportune structural design for effective steering and separation of charge carriers. In addition, a similar decay of photocurrent was observed for all the composite samples when the light source was cut off. This phenomenon can be ascribed to the slow discharge of accumulated charges from the middle layer of electrodes [50], suggesting the presence of electron reservoirs in our developed photocatalytic systems.

To further disclose the mechanistic origin resulting in the differences in activity over photocatalysts, electrochemical impedance spectroscopy (EIS) Nyquist plots of the samples were investigated. Generally, a smaller arc radius of the Nyquist plot reflects a lower electron transfer resistance and a better separation of photoinduced charge carriers, which result in a faster interfacial charge transfer process [51–54]. As depicted in Fig. 4B, BWO-OV/BOI displayed a much depressed arc radius compared to other samples, implying that BWO-OV/BOI possesses supreme electro-conductivity which significantly enhance the separation and migration of photoinduced charge carriers. This is mainly attributed to the presence of surface OV defects in BWO-OV, as these defects can greatly improve the electrical conductivity of semiconductors [55]. Furthermore, aside from being a co-catalyst, BWO-OV also serves as a 2D electron-conductive platform for accepting and shuttling of electrons generated from bandgap excitation of BOI. In comparison, solitary BOI possessed an increased arc radius, which can be attributed to the absence of secondary component to act as a charge relay medium for retarding the recombination of charge carriers. Combining the observation from Fig. S5B, all the samples with different weight loadings of BWO-OV exhibited a similar trend to that of transient photocurrent responses and were in accordance with their photoactivities. These findings indicate that excessive loadings of BWO-OV may cause severe overlapping with BOI, which shielded incident light from reaching BOI surface for the generation of photoexcited charge carriers.

Since the separation and transportation of charge carriers are closely related to the band-edge positions, the electronic structures of our developed photocatalytic system were investigated to determine the flowchart of photoinduced charge carriers in the composite. Mott-Schottky analysis was performed for solitary BOI and BWO-OV, where the Mott-Schottky plots were plotted according to the following equations [56,57]:

For *p*-type semiconductor,

$$\frac{1}{C^2} = \frac{2}{e\varepsilon\varepsilon_0 N_A}\left(E_{fb} - E - \frac{k_B T}{e}\right) \tag{3}$$

For *n*-type semiconductor,

$$\frac{1}{C^2} = \frac{2}{e\varepsilon\varepsilon_0 N_D}\left(E - E_{fb} - \frac{k_B T}{e}\right) \tag{4}$$

where C is the capacitance of space charge layer, e is the electronic charge, ε is the dielectric constant of the semiconductor, ε_0 is the permittivity in vacuum, N_A and N_D are the number of acceptors and donors in *p*-type and *n*-type semiconductors, respectively, E_{fb} is the flat-band potential, E is the applied potential, K_B is the Boltzmann's constant and T is the absolute temperature. Hence, a plot of $1/C^2$ *vs.* E should yield a straight line, where E_{fb} can be determined from the intercept of *X*-axis.

Based on Fig. 4C and inset, the apparent positive and the negative slopes of the plots revealed that BWO-OV is an *n*-type semiconductor whereas BOI is a *p*-type semiconductor. Besides, the E_{fb} of BWO-OV and BOI were estimated to be *ca.* −1.14 and 0.98 V *vs.* Ag/AgCl, which are equivalent to −0.94 and 1.18 V *vs.* normal hydrogen electrode (NHE), respectively ($E_{NHE} = E_{Ag/AgCl} + 0.197$ V) [58]. Since the rule of thumb dictates that the E_{fb} are about 0.3 V below CB minimum (CBM) of *n*-type semiconductor and 0.3 V above VB maximum (VBM) of *p*-type semiconductor [59,60], the CBM of BWO-OV and VBM of BOI were determined as −1.24 and 1.48 V *vs.* NHE, respectively. Working in tandem with the bandgap energies obtained from Tauc plots, the estimated electronic band structures of BWO-OV/BOI composite was delineated in Fig. 5A. As revealed by our UV–Vis absorption spectra, the long absorption tail of BWO-OV indicates that OV-induced defect states are judiciously positioned below the CB. The band tails of these mid-gap states can be determined from the Urbach plot, which is expressed as [61]:

$$\alpha = \alpha_o \exp\left(\frac{h\nu}{Eu}\right) \tag{5}$$

where α is the absorption coefficient, α_o is a constant, $h\nu$ denotes the incident photon energy and Eu is the Urbach energy which refers to the energy of band tail. Thus, the Eu value can be estimated from the inverse of slope of the ln α *vs.* $h\nu$ plot. From the Urbach plot (Fig. S6), the

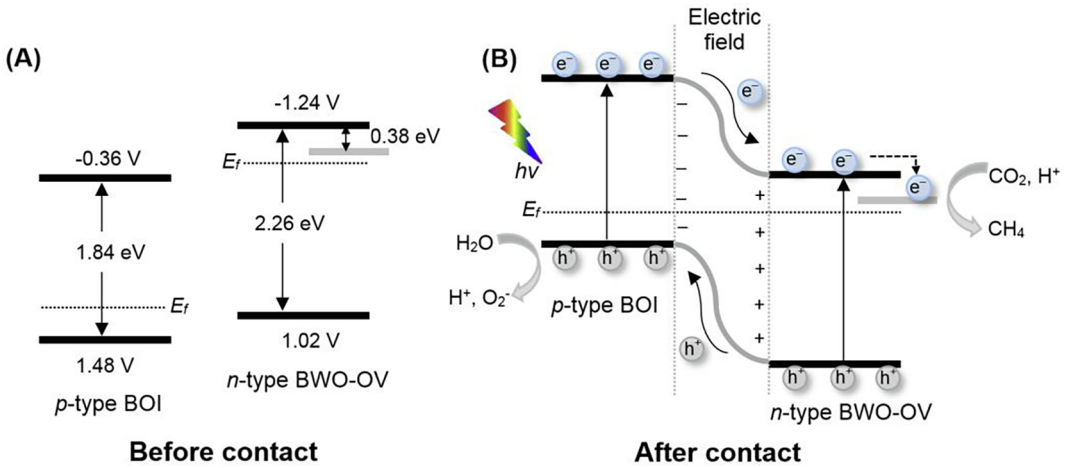

Fig. 5. (A) Estimated relative band positions and (B) Schematic diagram of charge transfer and separation at the *p*-*n* heterojunction in surface defect-engineered BWO-OV/BOI composite for photocatalytic CO_2 reduction.

Eu value was determined to be 0.38 eV, which signifies the gap from CBM to the OV-induced defect states of BWO-OV (Fig. 5A).

It is worth highlighting that the characteristic feature of *p-n* heterojunction is clearly observed from the Mott-Schottky plot of BWO-OV/BOI composite (Fig. 4D), in which an inverted V-shaped curve is shown [62]. This finding is of paramount significance, as the presence of *p-n* heterojunction has been known to greatly enhance the performance of photocatalytic systems through their rapid transfer of charge carriers across the built-in electrical field at the interface. As extensively documented, the Fermi level (E_f) of *p*-type semiconductor locates near to the VB whereas E_f exists close to the CB for *n*-type semiconductor [31]. Thus, the E_f of BWO-OV (*n*-type semiconductor) is higher than BOI (*p*-type semiconductor) in this case (Fig. 5A). When these two components come into contact, a favourable *p-n* heterojunction is formed, as illustrated in Fig. 5B. The difference in Fermi energy levels allows the diffusion of electrons from BWO-OV to BOI while holes to diffuse from BOI to BWO-OV. Consequently, positive charges accumulate at the BWO-OV and negative charges gather at BOI. Accompanying the electron-hole pairs diffusion, the energy bands of BOI shift upward along with its Fermi level, and those of BWO-OV shift downward until Fermi level equilibrium of the system is achieved. Thereafter, the regions close to the *p-n* heterointerface are charged, which leads to the formation of an internal electric field at the interface. Upon visible light irradiation, both the BWO-OV and BOI are photoexcited and photoinduced charge carriers are generated. This internal electric field functions to rapidly direct the holes in BWO-OV to BOI and electrons in BOI to migrate to BWO-OV. This electron transportation pathway is supported by our XPS results mentioned earlier, further affirming that the migration of charge carriers in this case is through *p-n* heterojunction instead of the conventional type II heterojunction, as the later will favour the electrons to transfer from BWO-OV to BOI instead due to their respective CB positions (Fig. 5A). It is worth highlighting that the hybrid photocatalysts with *p-n* heterojunction endow faster separation of charge carriers than the type II photocatalytic systems, owing to the cooperative synergy of internal electric field and energy band alignment [63].

Other than the positive contribution of *p-n* heterojunction, the imperative roles of OV defects played in the BWO-OV/BOI composite for photoactivity enhancement should not be neglected. After the directional migration of photogenerated electrons from BOI to CB of BWO-OV through *p-n* heterojunction, these electrons experience a second step electron transfer, which migrate from the CB of BWO-OV to the OV-defect states. This cascade electron transfer process with an ultimate goal of trapping the photoexcited electrons at the defect states can significantly boost the separation efficiency of electron-hole pairs, as evidenced by our observation from transient photocurrent responses and Nyquist plots. In the light of this, more photoexcited electrons can take part in the CO_2 photoreduction process. Coincidentally, theoretical calculations have revealed that the adsorption of CO_2 molecules is energetically favourable on the OV sites [29]. As reported in our previous works, once a CO_2 molecule adsorbs at the OV, the CO_2 molecule will be spontaneously activated into $\cdot CO_2^-$ radical through accepting a photoexcited electron from the OV site [23,24]. Since the reduction of CO_2 molecules is thermodynamically and kinetically favourable at the OVs, these $\cdot CO_2^-$ radicals would be further transformed into the desired CH_4 through multielectron transfer process. Of note, the attraction between CO_2 molecules and OVs can lead to the generation of unexpected affinity interactions, which greatly lower the energy barrier for interfacial charge transfer [64]. Thus, our deliberately inducing surface OV defects on BWO-OV presents as an elegant example to artificially tune and create more catalytic active sites for the targeted CO_2 photoreduction.

On the basis of above analysis, the proposed mechanism for photocatalytic CO_2 reduction over our novel 2D/2D BWO-OV/BOI binanosheets was elucidated in Fig. 6. Undoubtedly, the co-existence of nanoscale *p-n* heterojunction and surface defects in the BWO-OV/BOI cascade accounts for its superior photocatalytic performance. As widely accepted, a typical photocatalytic CO_2 reduction reaction involves three primary processes, which are: (i) photoabsorption; (ii) separation and transportation of photoinduced charge carriers; and (iii) CO_2 adsorption and activation by accepting photogenerated electrons [65]. Herein, our rational design and nanoscale-level control over architectures and electronic structures allow this photocatalytic system to fully optimize all the above-mentioned crucial processes. Firstly, the presence of OVs significantly alter the optical properties of Bi_2WO_6. Through excellent spectral coupling with BiOI, our developed BWO-OV/BOI composites are responsive for a broad spectrum of solar light, ranging from UV to NIR region, which is evidenced from the UV–Vis absorption results. Besides, this 2D/2D motif with built-in internal electric field resulting from the *p-n* heterojunction allows directional migration and spatial separation of photoinduced charge carriers to opposite sides of the heterostructure to hinder their recombination. Different from BOB-OV/BOI-Mix sample which lack of electron shuttle pathway between two adjacent components, this BOB-OV/BOI hybrid sample effectively utilize the built-in *p-n* heterojunction as interfacial charge flow highway to facilitate the transportation of electrons from BOI to BWO-OV. Furthermore, the cascade electron transfer in this system endows oxygen vacant sites on BWO-OV to serve as electron accumulated sites, which

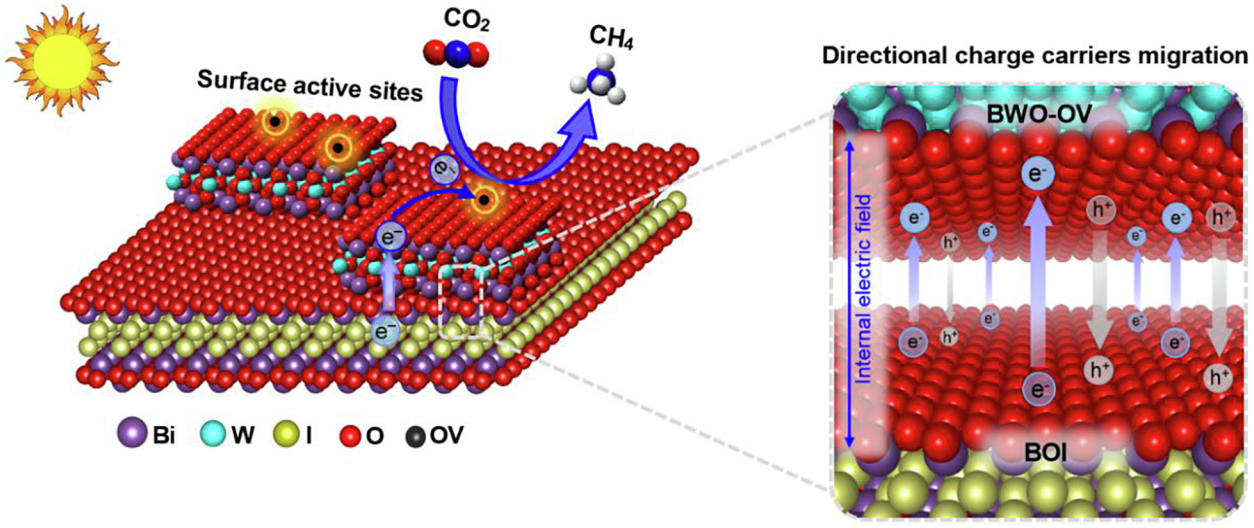

Fig. 6. Schematic illustration for the proposed mechanism of photocatalytic CO_2 reduction over the as-developed BWO-OV/BOI nanocomposite.

not only hamper the recombination of charge carriers, but also act as CO_2 adsorption and activation centres to initiate the CO_2 photoreduction processes. Benefitting from these remarkable features, our novel BOB-OV/BOI, despite being noble-metal-free, still exhibited superior photocatalytic CO_2 reduction activity. Considering its simple dual-components photocatalytic system and facile synthesis, we believe that this 2D/2D motif through rationally integrating oxygen-deficient Bi_2WO_6 nanosheets with BiOI nanosheets possesses great potential for a myriad of solar-to-chemical energy applications.

4. Conclusions

In summary, we have developed a novel 2D/2D BWO-OV/BOI photocatalytic system with co-existence of *p-n* heterojunction and surface oxygen vacancy defects. This nanoscale-level of structural and interfacial design enabled us to effectively manipulate the generation, separation, transportation and consumption of charge carriers. With the successful controlling and steering of charge flow, this photocatalytic system offered a remarkable CH_4 production yield of 18.32 μmol/g, superior to any hitherto reported 2D BiOI-based or Bi_2WO_6-based photocatalysts with the application of visible light-driven CH_4 production. We believe that our work breathes new life into photocatalysis, as the opportune structural and interfacial design offered access to the nanoscale-level understanding of charge flow manipulation and utilization for achieving greatly enhanced photocatalytic performance.

Acknowledgements

This work was funded by the Ministry of Higher Education (MOHE) Malaysia and Universiti Sains Malaysia (USM) under NanoMITe Long-term Research Grant Scheme (LRGS) (Ref. no.: 203/PJKIMIA/6720009).

Appendix A. Supplementary data

Supplementary data to this article can be found online at https://doi.org/10.1016/j.cej.2019.05.001.

References

[1] K. Li, B. Peng, T. Peng, Recent advances in heterogeneous photocatalytic CO_2 conversion to solar fuels, ACS Catal. 6 (2016) 7485–7527, https://doi.org/10.1021/acscatal.6b02089.

[2] W. Tu, Y. Zhou, Z. Zou, Photocatalytic conversion of CO_2 into renewable hydrocarbon fuels: state-of-the-art accomplishment, challenges, and prospects, Adv. Mater. 26 (2014) 4607–4626, https://doi.org/10.1002/adma.201400087.

[3] J.-Y. Tang, X.Y. Kong, B.-J. Ng, Y.-H. Chew, A.R. Mohamed, S.-P. Chai, Midgap-state-mediated two-steps photoexcitation in nitrogen defective g-C_3N_4 atomic layers for superior photocatalytic CO_2 reduction, Catal. Sci. Technol. (2019), https://doi.org/10.1039/C9CY00449A.

[4] L. Zhang, W. Wang, D. Jiang, E. Gao, S. Sun, Photoreduction of CO_2 on BiOCl nanoplates with the assistance of photoinduced oxygen vacancies, Nano Res. 8 (2015) 821–831, https://doi.org/10.1007/s12274-014-0564-2.

[5] J.L. White, M.F. Baruch, J.E. Pander III, Y. Hu, I.C. Fortmeyer, J.E. Park, T. Zhang, K. Liao, J. Gu, Y. Yan, T.W. Shaw, E. Abelev, A.B. Bocarsly, Light-driven heterogeneous reduction of carbon dioxide: photocatalysts and photoelectrodes, Chem. Rev. 115 (2015) 12888–12935, https://doi.org/10.1021/acs.chemrev.5b00370.

[6] G. Zhao, W. Zhou, Y. Sun, X. Wang, H. Liu, X. Meng, K. Chang, J. Ye, Efficient photocatalytic CO_2 reduction over Co(II) species modified CdS in aqueous solution, Appl. Catal., B 226 (2018) 252–257, https://doi.org/10.1016/j.apcatb.2017.12.054.

[7] J. Hou, S. Cao, Y. Wu, F. Liang, Y. Sun, Z. Lin, L. Sun, Simultaneously efficient light absorption and charge transport of phosphate and oxygen-vacancy confined in bismuth tungstate atomic layers triggering robust solar CO_2 reduction, Nano Energy 32 (2017) 359–366, https://doi.org/10.1016/j.nanoen.2016.12.054.

[8] M. Tahir, N.S. Amin, Indium-doped TiO_2 nanoparticles for photocatalytic CO_2 reduction with H_2O vapors to CH_4, Appl. Catal., B 162 (2015) 98–109, https://doi.org/10.1016/j.apcatb.2014.06.037.

[9] M. Zhou, S. Wang, P. Yang, Z. Luo, R. Yuan, A.M. Asiri, M. Wakeel, X. Wang, Layered heterostructures of ultrathin polymeric carbon nitride and $ZnIn_2S_4$ nanosheets for photocatalytic CO_2 reduction, Chem. Eur. J. 24 (2018) 18529–18534, https://doi.org/10.1002/chem.201803250.

[10] S. Wang, B.Y. Guan, Y. Lu, X.W. "David" Lou, Formation of hierarchical In_2S_3–$CdIn_2S_4$ heterostructured nanotubes for efficient and stable visible light CO_2 reduction, J. Am. Chem. Soc. 139 (2017) 17305–17308, https://doi.org/10.1021/jacs.7b10733.

[11] A. Kumar, A. Kumar, G. Sharma, A.H. Al-Muhtaseb, M. Naushad, A.A. Ghfar, C. Guo, F.J. Stadler, Biochar-templated g-C_3N_4/$Bi_2O_2CO_3$/$CoFe_2O_4$ nano-assembly for visible and solar assisted photo-degradation of paraquat, nitrophenol reduction and CO_2 conversion, Chem. Eng. J. 339 (2018) 393–410, https://doi.org/10.1016/j.cej.2018.01.105.

[12] F. Chen, H. Huang, L. Ye, T. Zhang, Y. Zhang, X. Han, T. Ma, Thickness-dependent facet junction control of layered $BiOIO_3$ single crystals for highly efficient CO_2 photoreduction, Adv. Funct. Mater. 28 (2018) 1804284, https://doi.org/10.1002/adfm.201804284.

[13] V.P. Indrakanti, J.D. Kubicki, H.H. Schobert, Photoinduced activation of CO_2 on TiO_2 surfaces: quantum chemical modeling of CO_2 adsorption on oxygen vacancies, Energy Environ. Sci. 2 (2009) 745–758, https://doi.org/10.1016/j.fuproc.2010.09.007.

[14] J. Li, G. Zhan, Y. Yu, L. Zhang, Superior visible light hydrogen evolution of Janus bilayer junctions *via* atomic-level charge flow steering, Nat. Commun. 7 (2016) 11480, https://doi.org/10.1038/ncomms11480.

[15] Y. Wang, L. Zhang, K. Cui, C. Xu, H. Li, H. Liu, J. Yu, Solar driven electrochromic photoelectrochemical fuel cells for simultaneous energy conversion, storage and self-powered sensing, Nanoscale 10 (2018) 3421–3428, https://doi.org/10.1039/c7nr09275j.

[16] R. He, D. Xu, B. Cheng, J. Yu, W. Ho, Review on nanoscale bi-based photocatalysts, Nanoscale Horizons. 3 (2018) 464–504, https://doi.org/10.1039/C8NH00062J.

[17] J. Di, J. Xia, H. Li, S. Guo, S. Dai, Bismuth oxyhalide layered materials for energy and environmental applications, Nano Energy 41 (2017) 172–192, https://doi.org/10.1016/j.nanoen.2017.09.008.

[18] L. Ye, Y. Su, X. Jin, H. Xie, C. Zhang, Recent advances in BiOX (X = Cl, Br and I) photocatalysts: synthesis, modification, facet effects and mechanisms, Environ. Sci. Nano 1 (2014) 90–112, https://doi.org/10.1039/c3en00098b.

[19] H. Wang, H. Ye, B. Zhang, F. Zhao, B. Zeng, Electrostatic interaction mechanism based synthesis of a Z-scheme BiOI – CdS photocatalyst for selective and sensitive detection of Cu^{2+}, J. Mater. Chem. A 5 (2017) 10599–10608, https://doi.org/10.1039/C7TA02691A.

[20] S. Wang, B.Y. Guan, X. Wang, X.W.D. Lou, Formation of hierarchical Co_9S_8@$ZnIn_2S_4$ heterostructured cages as an efficient photocatalyst for hydrogen evolution, J. Am. Chem. Soc. 140 (2018) 15145–15148, https://doi.org/10.1021/jacs.8b07721.

[21] N. Zhang, R. Ciriminna, M. Pagliaro, Y.-J. Xu, Nanochemistry-derived Bi_2WO_6 nanostructures: towards production of sustainable chemicals and fuels induced by visible light, Chem. Soc. Rev. 43 (2014) 5276–5287, https://doi.org/10.1039/c4cs00056k.

[22] L. Liang, F. Lei, S. Gao, Y. Sun, X. Jiao, J. Wu, S. Qamar, Y. Xie, Single unit cell bismuth tungstate layers realizing robust solar CO_2 reduction to methanol, Angew. Chem. Int. Ed. 54 (2015) 13971–13974, https://doi.org/10.1002/anie.201506966.

[23] X.Y. Kong, Y.Y. Choo, S.-P. Chai, A.K. Soh, A.R. Mohamed, Oxygen vacancy induced Bi_2WO_6 for the realization of photocatalytic CO_2 reduction over the full solar spectrum: from the UV to the NIR region, Chem. Commun. 52 (2016) 14242–14245, https://doi.org/10.1039/C6CC07750A.

[24] W.-J. Ong, L.-L. Tan, Y.H. Ng, S.-T. Yong, S.-P. Chai, Graphitic carbon nitride (g-C_3N_4)-based photocatalysts for artificial photosynthesis and environmental remediation: are we a step closer to achieving sustainability? Chem. Rev. 116 (2016) 7159–7329.

[25] X.Y. Kong, W.P.C. Lee, W.J. Ong, S.P. Chai, A.R. Mohamed, Oxygen-deficient BiOBr as a highly stable photocatalyst for efficient CO_2 reduction into renewable carbon-neutral fuels, ChemCatChem 8 (2016) 3074–3081, https://doi.org/10.1002/cctc.201600782.

[26] W.-J. Ong, L.-L. Tan, S.-P. Chai, S.-T. Yong, A.R. Mohamed, Highly reactive 001 facets of TiO2-based composites: synthesis, formation mechanism and characterization, Nanoscale 6 (2014) 1946–2008, https://doi.org/10.1039/c3nr04655a.

[27] H. Zhang, J. Cai, Y. Wang, M. Wu, M. Meng, Y. Tian, X. Li, J. Zhang, L. Zheng, Z. Jiang, J. Gong, Insights into the effects of surface/bulk defects on photocatalytic hydrogen evolution over TiO_2 with exposed {001} facets, Appl. Catal., B 220 (2018) 126–136, https://doi.org/10.1016/j.apcatb.2017.08.046.

[28] F. Chen, H. Huang, L. Guo, Y. Zhang, T. Ma, The role of polarization in photocatalysis, Angew. Chemie Int. Ed. (n.d.). doi:10.1002/anie.201901361.

[29] L. Liu, C. Zhao, Y. Li, Spontaneous dissociation of CO_2 to CO on defective surface of Cu(I)/TiO_{2-x} nanoparticles at room temperature, J. Phys. Chem. C 116 (2012) 7904–7912, https://doi.org/10.1021/jp300932b.

[30] H. Yu, J. Li, Y. Zhang, S. Yang, K. Han, F. Dong, T. Ma, H. Huang, Three-in-one oxygen vacancies: whole visible-spectrum absorption, efficient charge separation, and surface site activation for robust CO_2 photoreduction, Angew. Chem. Int. Ed. 58 (2019) 3880–3884, https://doi.org/10.1002/anie.201813967.

[31] L.K. Putri, B.-J. Ng, W.-J. Ong, H.W. Lee, W.S. Chang, S.-P. Chai, Engineering nanoscale p–n junction *via* the synergetic dual-doping of p-type boron-doped graphene hybridized with n-type oxygen-doped carbon nitride for enhanced photocatalytic hydrogen evolution, J. Mater. Chem. A 6 (2018) 3181–3194, https://doi.org/10.1039/C7TA09723A.

[32] S. Liu, C. Han, Z. Tang, Y. Xu, Heterostructured semiconductor nanowire arrays for artificial photosynthesis, Mater. Horizons. 3 (2016) 270–282, https://doi.org/10.1039/c6mh00063k.

[33] H. Huang, K. Xiao, Y. He, T. Zhang, F. Dong, X. Du, Y. Zhang, In situ assembly of BiOI@Bi12O17Cl2 p-n junction: charge induced unique front-lateral surfaces coupling heterostructure with high exposure of BiOI 001 active facets for robust and nonselective photocatalysis, Appl. Catal., B 199 (2016) 75–86, https://doi.org/10.

1016/j.apcatb.2016.06.020.
[34] F. Dong, T. Xiong, Y. Sun, Y. Zhang, Y. Zhou, Controlling interfacial contact and exposed facets for enhancing photocatalysis *via* 2D–2D heterostructures, Chem. Commun. 51 (2015) 8249–8252, https://doi.org/10.1039/C5CC01993A.
[35] Y. Zhou, Z. Tian, Z. Zhao, Q. Liu, J. Kou, X. Chen, J. Gao, S. Yan, Z. Zou, High-yield synthesis of ultrathin and uniform Bi_2WO_6 square nanoplates benefitting from photocatalytic reduction of CO_2 into renewable hydrocarbon fuel under visible light, ACS Appl. Mater. Interfaces 3 (2011) 3594–3601.
[36] X.Y. Kong, W.L. Tan, B. Ng, S. Chai, A.R. Mohamed, Harnessing Vis–NIR broad spectrum for photocatalytic CO_2 reduction over carbon quantum dots-decorated ultrathin Bi_2WO_6 nanosheets, Nano Res. 10 (2017) 1720–1731, https://doi.org/10.1007/s12274-017-1435-4.
[37] Z. Liu, B. Wu, Y. Zhu, D. Yin, L. Wang, Fe-ions modified biobr mesoporous microspheres with excellent photocatalytic property, Catal. Lett. 142 (2012) 1489–1497, https://doi.org/10.1007/s10562-012-0899-9.
[38] H. Li, J. Shi, K. Zhao, L. Zhang, Sustainable molecular oxygen activation with oxygen vacancies on the 001 facets of BiOCl nanosheets under solar light, Nanoscale 6 (2014) 14168–14173, https://doi.org/10.1039/c4nr04810e.
[39] W.-K. Jo, J.Y. Lee, T.S. Natarajan, Fabrication of hierarchically structured novel redox-mediator-free $ZnIn_2S_4$ marigold flower/ Bi_2WO_6 flower-like direct Z-scheme nanocomposite photocatalysts with superior visible light photocatalytic efficiency, Phys. Chem. Chem. Phys. 18 (2016) 1000–1016, https://doi.org/10.1039/C5CP06176H.
[40] J. Low, C. Jiang, B. Cheng, S. Wageh, A.A. Al-ghamdi, J. Yu, A review of direct Z-scheme photocatalysts, Small Methods 1 (2017) 1700080, https://doi.org/10.1002/smtd.201700080.
[41] W. Yu, D. Xu, T. Peng, Enhanced photocatalytic activity of g-C_3N_4 for selective CO_2 reduction to CH_3OH *via* facile coupling of ZnO: a direct Z-scheme mechanism, J. Mater. Chem. A 3 (2015) 19936–19947, https://doi.org/10.1039/C5TA05503B.
[42] M. Lyu, J. Yun, M. Cai, Y. Jiao, P.V. Bernhardt, M. Zhang, Q. Wang, A. Du, H. Wang, G. Liu, L. Wang, Organic–inorganic bismuth (III)-based material: a lead- free, air-stable and solution-processable light-absorber beyond organolead perovskites, Nano Res. 9 (2016) 692–702, https://doi.org/10.1007/s12274-015-0948-y.
[43] G. Xi, S. Ouyang, P. Li, J. Ye, Q. Ma, N. Su, H. Bai, C. Wang, Ultrathin $W_{18}O_{49}$ nanowires with diameters below 1 nm: synthesis, near-infrared absorption, photoluminescence, and photochemical reduction of carbon dioxide, Angew. Chem. Int. Ed. 51 (2012) 2395–2399, https://doi.org/10.1002/anie.201107681.
[44] X.Y. Kong, B.J. Ng, K.H. Tan, X. Chen, H. Wang, A.R. Mohamed, S.P. Chai, Simultaneous generation of oxygen vacancies on ultrathin BiOBr nanosheets during visible-light-driven CO_2 photoreduction evoked superior activity and long-term stability, Catal. Today 314 (2018) 20–27, https://doi.org/10.1016/j.cattod.2018.04.018.
[45] B. Ng, L.K. Putri, X.Y. Kong, K.P.Y. Shak, P. Pasbakhsh, S.-P. Chai, A.R. Mohamed, Sub-2nm Pt-decorated $Zn_{0.5}Cd_{0.5}S$ nanocrystals with twin-induced homojuntions for efficient visible-light-driven photocatalytic H_2 evolution, Appl. Catal., B 224 (2018) 360–367, https://doi.org/10.1016/j.apcatb.2017.10.005.
[46] S. Wang, X. Wang, Photocatalytic CO_2 reduction by CdS promoted with a zeolitic imidazolate framework, Appl. Catal., B 162 (2015) 494–500, https://doi.org/10.1016/j.apcatb.2014.07.026.
[47] J. Peng, J. Xu, Z. Wang, Z. Ding, S. Wang, Developing an efficient $NiCo_2S_4$ cocatalyst for improving the visible light H_2 evolution performance of CdS nanoparticles, Phys. Chem. Chem. Phys. 19 (2017) 25919–25926, https://doi.org/10.1039/c7cp05147f.
[48] W.P.C. Lee, X.Y. Kong, L.L. Tan, M.M. Gui, S. Sumathi, S.P. Chai, Molybdenum disulfide quantum dots decorated bismuth sulfide as a superior noble-metal-free photocatalyst for hydrogen evolution through harnessing a broad solar spectrum, Appl. Catal., B 232 (2018) 117–123, https://doi.org/10.1016/j.apcatb.2018.03.019.
[49] S. Wang, B.Y. Guan, X.W.D. Lou, Construction of $ZnIn_2S_4$-In_2O_3 hierarchical tubular heterostructures for efficient CO_2 photoreduction, J. Am. Chem. Soc. 140 (2018) 5037–5040, https://doi.org/10.1021/jacs.8b02200.
[50] L. Yuan, B. Weng, J.C. Colmenares, Y. Sun, Y.J. Xu, Multichannel charge transfer and mechanistic insight in metal decorated 2D–2D Bi_2WO_6–TiO_2 cascade with enhanced photocatalytic performance, Small 13 (2017) 1702253, https://doi.org/10.1002/smll.201702253.
[51] Q. Quan, S. Xie, B. Weng, Y. Wang, Y. Xu, Revealing the double-edged sword role of graphene on boosted charge transfer versus active site control in TiO_2 nanotube arrays@RGO/MoS_2 heterostructure, Small 1704531 (2018), https://doi.org/10.1002/smll.201704531.
[52] L. Sun, L. Xiang, X. Zhao, C.J. Jia, J. Yang, Z. Jin, X. Cheng, W. Fan, Enhanced visible-light photocatalytic activity of bioi/biocl heterojunctions: key role of crystal facet combination, ACS Catal. 5 (2015) 3540–3551, https://doi.org/10.1021/cs501631n.
[53] J. Xu, C. Sun, Z. Wang, Y. Hou, Z. Ding, S. Wang, Perovskite oxide $LaNiO_3$ nanoparticles for boosting H_2 evolution over commercial CdS with visible light, Chem. Eur. J. 24 (2018) 18512–18517, https://doi.org/10.1002/chem.201802920.
[54] M. Zhou, S. Wang, P. Yang, C. Huang, X. Wang, Boron carbon nitride semiconductors decorated with CdS nanoparticles for photocatalytic reduction of CO_2, ACS Catal. 8 (2018) 4928–4936, https://doi.org/10.1021/acscatal.8b00104.
[55] M. Salari, K. Konstantinov, H.K. Liu, Enhancement of the capacitance in TiO_2 nanotubes through controlled introduction of oxygen vacancies, J. Mater. Chem. 21 (2011) 5128–5133, https://doi.org/10.1039/c0jm04085a.
[56] S. Bai, J. Jiang, Q. Zhang, Y. Xiong, Steering charge kinetics in photocatalysis: intersection of materials syntheses, characterization techniques and theoretical simulations, Chem. Soc. Rev. 44 (2015) 2893–2939, https://doi.org/10.1039/C5CS00064E.
[57] J. Shang, W. Hao, X. Lv, T. Wang, X. Wang, Y. Du, S. Dou, T. Xie, D. Wang, J. Wang, Bismuth oxybromide with reasonable photocatalytic reduction activity under visible light, ACS Catal. 4 (2014) 954–961, https://doi.org/10.1021/cs401025u.
[58] K. Okazaki, Y. Nakato, K. Murakoshi, Absolute potential of the Fermi level of isolated single-walled carbon nanotubes, Phys. Rev. B 68 (2003) 035434, , https://doi.org/10.1103/PhysRevB.68.035434.
[59] W. Yin, L. Bai, Y. Zhu, S. Zhong, L. Zhao, Z. Li, S. Bai, Embedding metal in the interface of a p-n heterojunction with a stack design for superior Z-scheme photocatalytic hydrogen evolution, ACS Appl. Mater. Interfaces 8 (2016) 23133–23142, https://doi.org/10.1021/acsami.6b07754.
[60] H. Huang, X. Li, J. Wang, F. Dong, P.K. Chu, T. Zhang, Y. Zhang, Anionic group self-doping as a promising strategy: band-gap engineering and multi-functional applications of high-performance CO_{32}-doped $Bi_2O_2CO_3$, ACS Catal. 5 (2015) 4094–4103, https://doi.org/10.1021/acscatal.5b00444.
[61] F. Urbach, The long-wavelength edge of photographic sensitivity and of the electronic absorption of solids, Phys. Rev. 92 (1953) 1324, https://doi.org/10.1103/PhysRev. 92.1324.
[62] F. Meng, J. Li, S.K. Cushing, M. Zhi, N. Wu, Solar hydrogen generation by nanoscale p-n junction of p-type molybdenum disulfide/n-type nitrogen-doped reduced graphene oxide, J. Am. Chem. Soc. 135 (2013) 10286–10289, https://doi.org/10.1021/ja404851s.
[63] J. Low, J. Yu, M. Jaroniec, S. Wageh, A.A. Al-ghamdi, Heterojunction photocatalysts, Adv. Mater. 29 (2017) 1601694, https://doi.org/10.1002/adma.201601694.
[64] V.P. Indrakanti, H.H. Schobert, J.D. Kubicki, Quantum mechanical modeling of CO_2 interactions with irradiated stoichiometric and oxygen-deficient anatase TiO_2 surfaces: implications for the photocatalytic reduction of CO_2, Energy Fuels 23 (2009) 5247–5256, https://doi.org/10.1021/ef9003957.
[65] X. Jiao, Z. Chen, X. Li, Y. Sun, S. Gao, W. Yan, C. Wang, Q. Zhang, Y. Lin, Y. Luo, Y. Xie, Defect-mediated electron-hole separation in one-unit-cell $ZnIn_2S_4$ layers for boosted solar-driven CO_2 reduction, J. Am. Chem. Soc. 139 (2017) 7586–7594, https://doi.org/10.1021/jacs.7b02290.